

## REPORT DOCUMENTATION PAGE

Form Approved OMB NO. 0704-0188

The public reporting burden for this collection of information is estimated to average 1 hour per response, including the time for reviewing instructions, searching existing data sources, gathering and maintaining the data needed, and completing and reviewing the collection of information. Send comments regarding this burden estimate or any other aspect of this collection of information, including suggestions for reducing this burden, to Washington Headquarters Services, Directorate for Information Operations and Reports, 1215 Jefferson Davis Highway, Suite 1204, Arlington VA 22202-4302. Respondents should be aware that notwithstanding any other provision of law, no person shall be subject to any penalty for failing to comply with a collection of information if it does not display a currently valid OMB control number.  
PLEASE DO NOT RETURN YOUR FORM TO THE ABOVE ADDRESS.

1. REPORT DATE (DD-MM-YYYY) 11-08-2015	2. REPORT TYPE Final Report	3. DATES COVERED (From - To) 15-Apr-2012 - 14-Apr-2015		
4. TITLE AND SUBTITLE Final Report: Symmetry mismatched heterostructures: New routes to bandwidth control in oxides		5a. CONTRACT NUMBER W911NF-12-1-0132		
		5b. GRANT NUMBER		
		5c. PROGRAM ELEMENT NUMBER 611102		
6. AUTHORS Steven May		5d. PROJECT NUMBER		
		5e. TASK NUMBER		
		5f. WORK UNIT NUMBER		
7. PERFORMING ORGANIZATION NAMES AND ADDRESSES Drexel University Office of Research 3201 Arch Street, Suite 100 Philadelphia, PA 19104 -2875		8. PERFORMING ORGANIZATION REPORT NUMBER		
9. SPONSORING/MONITORING AGENCY NAME(S) AND ADDRESS (ES) U.S. Army Research Office P.O. Box 12211 Research Triangle Park, NC 27709-2211		10. SPONSOR/MONITOR'S ACRONYM(S) ARO		
		11. SPONSOR/MONITOR'S REPORT NUMBER(S) 61954-PH-YIP.16		
12. DISTRIBUTION AVAILABILITY STATEMENT Approved for Public Release; Distribution Unlimited				
13. SUPPLEMENTARY NOTES The views, opinions and/or findings contained in this report are those of the author(s) and should not be construed as an official Department of the Army position, policy or decision, unless so designated by other documentation.				
14. ABSTRACT This project aims to discover novel physical phenomena in correlated ABO <sub>3</sub> oxide heterostructures by using interfacial coupling to control the behavior of BO <sub>6</sub> octahedra, the connectivity of which are directly coupled to electronic bandwidth. Work on ultrathin La <sub>2</sub> /3Sr <sub>1</sub> /3MnO <sub>3</sub> films grown on LSAT and NdGaO <sub>3</sub> substrates, which have the same lattice parameters but different crystal symmetry, has revealed a systematic divergence in properties as the film thickness is reduced. This study is a direct demonstration of how octahedral imprinting contributes significantly to nanoscale bandgap control and provides insight into the length scale associated with interfacial				
15. SUBJECT TERMS correlated electron systems, oxide heterostructures, epitaxy, octahedral rotations				
16. SECURITY CLASSIFICATION OF: a. REPORT UU		17. LIMITATION OF ABSTRACT UU	15. NUMBER OF PAGES	19a. NAME OF RESPONSIBLE PERSON Steven May
b. ABSTRACT UU		c. THIS PAGE UU		19b. TELEPHONE NUMBER 215-571-3650



## Report Title

Final Report: Symmetry mismatched heterostructures: New routes to bandwidth control in oxides

### ABSTRACT

This project aims to discover novel physical phenomena in correlated ABO<sub>3</sub> oxide heterostructures by using interfacial coupling to control the behavior of BO<sub>6</sub> octahedra, the connectivity of which are directly coupled to electronic bandwidth. Work on ultrathin La<sub>2</sub>/3Sr<sub>1</sub>/3MnO<sub>3</sub> films grown on LSAT and NdGaO<sub>3</sub> substrates, which have the same lattice parameters but different crystal symmetry, has revealed a systematic divergence in properties as the film thickness is reduced. This study is a direct demonstration of how octahedral imprinting contributes significantly to properties at oxide interfaces, and provides insight into the length scale associated with interfacial octahedral coupling. A second goal of the project is to investigate structural coupling effects in isovalent complex oxide superlattices, allowing for the isolation of electronic effects driven by octahedral coupling. To this end, our work on La<sub>0.7</sub>Sr<sub>0.3</sub>MnO<sub>3</sub>/Eu<sub>0.7</sub>Sr<sub>0.3</sub>MnO<sub>3</sub> superlattices has provided the first direct experimental demonstration of how octahedral behavior in oxide heterostructures can be used to engineer spatially confined or uniform macroscopic properties by varying the superlattice period with respect to the length scale of interfacial structural coupling. By varying the wavelength and amplitude of the octahedral modulations, a transition is induced from modulated magnetization in large-period superlattices to homogeneous magnetization in short-period superlattices.

---

**Enter List of papers submitted or published that acknowledge ARO support from the start of the project to the date of this printing. List the papers, including journal references, in the following categories:**

**(a) Papers published in peer-reviewed journals (N/A for none)**

<u>Received</u>	<u>Paper</u>
02/12/2014	4.00 Eun Ju Moon, Yujun Xie, Eric D. Laird, David J. Keavney, Christopher Y. Li, Steven J. May. Fluorination of Epitaxial Oxides: Synthesis of Perovskite Oxyfluoride Thin Films, Journal of the American Chemical Society, (02 2014): 2224. doi: 10.1021/ja410954z
05/15/2014	7.00 E. J. Moon, P. V. Balachandran, B. J. Kirby, D. J. Keavney, R. J. Sichel-Tissot, C. M. Schlepütz, E. Karapetrova, X. M. Cheng, J. M. Rondinelli, S. J. May. Effect of Interfacial Octahedral Behavior in Ultrathin Manganite Films, Nano Letters, (05 2014): 2509. doi: 10.1021/nl500235f
06/30/2014	8.00 Eun Ju Moon, David J. Keavney, Steven J. May. Strain Effects in Narrow-Bandwidth Manganites: The Case of Epitaxial Eu <sub>0.7</sub> Sr <sub>0.3</sub> MnO <sub>3</sub> Thin Films, PHYSICAL REVIEW Applied, (06 2014): 54006. doi: 10.1103/PhysRevApplied.1.054006
07/10/2014	9.00 Anand Bhattacharya, Steven J. May. Magnetic Oxide Heterostructures, Annual Review of Materials Research, (07 2014): 65. doi: 10.1146/annurev-matsci-070813-113447
07/29/2015	14.00 E. J. Moon, A. K. Choquette, A. Huon, S. Z. Kulesa, D. Barbash, S. J. May. Comparison of topotactic fluorination methods for complex oxide films, APL Materials, (06 2015): 62511. doi: 10.1063/1.4921579
12/15/2014	11.00 R. Colby, Q. Wang, E. Karapetrova, E. J. Moon, C. M. Schlepütz, M. R. Fitzsimmons, S. J. May. Spatial control of functional properties via octahedral modulations in complex oxide superlattices, Nature Communications, (12 2014): 5710. doi: 10.1038/ncomms6710

02/12/2014	4.00 Eun Ju Moon, Yujun Xie, Eric D. Laird, David J. Keavney, Christopher Y. Li, Steven J. May. Fluorination of Epitaxial Oxides: Synthesis of Perovskite Oxyfluoride Thin Films, Journal of the American Chemical Society, (02 2014): 2224. doi: 10.1021/ja410954z
05/15/2014	7.00 E. J. Moon, P. V. Balachandran, B. J. Kirby, D. J. Keavney, R. J. Sichel-Tissot, C. M. Schlepütz, E. Karapetrova, X. M. Cheng, J. M. Rondinelli, S. J. May. Effect of Interfacial Octahedral Behavior in Ultrathin Manganite Films, Nano Letters, (05 2014): 2509. doi: 10.1021/nl500235f
06/30/2014	8.00 Eun Ju Moon, David J. Keavney, Steven J. May. Strain Effects in Narrow-Bandwidth Manganites: The Case of Epitaxial Eu <sub>0.7</sub> Sr <sub>0.3</sub> MnO <sub>3</sub> Thin Films, PHYSICAL REVIEW Applied, (06 2014): 54006. doi: 10.1103/PhysRevApplied.1.054006
07/10/2014	9.00 Anand Bhattacharya, Steven J. May. Magnetic Oxide Heterostructures, Annual Review of Materials Research, (07 2014): 65. doi: 10.1146/annurev-matsci-070813-113447
07/29/2015	14.00 E. J. Moon, A. K. Choquette, A. Huon, S. Z. Kulesa, D. Barbash, S. J. May. Comparison of topotactic fluorination methods for complex oxide films, APL Materials, (06 2015): 62511. doi: 10.1063/1.4921579
12/15/2014	11.00 R. Colby, Q. Wang, E. Karapetrova, E. J. Moon, C. M. Schlepütz, M. R. Fitzsimmons, S. J. May. Spatial control of functional properties via octahedral modulations in complex oxide superlattices, Nature Communications, (12 2014): 5710. doi: 10.1038/ncomms6710

**TOTAL:**

**6**

**Number of Papers published in peer-reviewed journals:**

---

**(b) Papers published in non-peer-reviewed journals (N/A for none)**

Received      Paper

08/11/2015 15.00 Q. He, R. Ishikawa , A.R. Lupini, L. Qiao, E.J. Moon, O. Ovchinnikov, S.J. May, M.D. Biegalski, A.Y. Borisevich. Towards 3D mapping of BO6 octahedron rotations at perovskite heterointerfaces, unit cell by unit cell,  
ACS Nano, (07 2015): 0. doi:

**TOTAL:**      **1**

**Number of Papers published in non peer-reviewed journals:**

---

**(c) Presentations**

\* denotes invited talk

ARO funding was acknowledged in all presentations.

- 1.\* “Measuring octahedral behavior in complex oxide heterostructures.” S. J. May, workshop on Future Directions for Emergent Discoveries at Oxide Interfaces by Design, Newport, RI, July 9-10, 2012.
- 2.\* “Measuring and controlling octahedral behavior in oxide heterostructures.” S. J. May, Complex Oxide Heterostructure Workshop at Harvard University, Cambridge, MA, August 8-9, 2012.
- 3.\* “Control of octahedral connectivity in oxide heterostructures” S. J. May, Materials Research Society fall meeting, Boston, MA, November 26 – 30, 2012.
4. “The effect of interfacial octahedral behavior on magnetic properties in ultrathin manganite films” E. J. Moon, X. Cheng, D. J. Keavney, and S. J. May. American Physical Society March meeting, Baltimore, MD, March 18 – 22, 2013.
5. “Fluorination of epitaxial oxides: Creating ferrite and nickelate oxyfluoride films” E. J. Moon, Y. J. Xie, D. J. Keavney, J. Goebel, E. D. Laird, C. Y. Li, and S. J. May. American Physical Society March meeting, Baltimore, MD, March 18 – 22, 2013.
- 6.\* “Anion-based approaches to tunable functionality in oxide heterostructures” S. J. May, Telluride Workshop on Competing Interactions and Colossal Responses in Transition Metal Compounds, Telluride, CO, July 15-19, 2013.
7. “Magnetic effect of interfacial octahedral behavior in ultrathin manganite films” E. J. Moon, B. J. Kirby, D. J. Keavney, P. V. Balachandran, R. J. Sichel-Tissot, C. M. Schlepütz, E. Karapetrova, X. M. Cheng, J. M. Rondinelli, and S. J. May. Magnetism and Magnetic Materials conference, Denver, CO. November 4-8, 2013.
8. “Strain-tailored magnetic properties of epitaxially grown ultrathin Eu<sub>0.7</sub>Sr<sub>0.3</sub>MnO<sub>3</sub> films” E. Moon, D. Keavney and S. May. Magnetism and Magnetic Materials conference, Denver, CO. November 4-8, 2013.
- 9.\* “The effect of interfacial octahedral behavior in ferromagnetic manganite heterostructures” E. J. Moon and S. J. May, American Ceramic Society Electronic Materials and Applications, Orlando, FL, January 22-24, 2014.
- 10.\* “Anion-based approaches to tunable functionality in oxide heterostructures” S. J. May, American Physical Society March meeting, Denver, CO, March 3-7, 2014.
- 11.\*“Anion-based approaches to tunable functionality in perovskite films and superlattices” S. J. May, 21st International Workshop on Oxide Electronics, Bolton Landing, NY, September 28-October 1, 2014.
12. “Spatial control of functional properties via octahedral modulations in complex oxide superlattices” E. J. Moon, R. Colby, Q. Wang, E. Karapetrova, C. M. Schleputz, M. R. Fitzsimmons, S. J. May. MRS Fall Meeting, Boston, MA, Dec. 1 – 4, 2014.
- 13.\*“Engineering anion positions and compositions in perovskite oxide heterostructures” S. J. May, International Conference on Electroceramics, State College, PA, May 13 – 16, 2015.
- 14.\*“Structural approaches for altering electronic and magnetic properties at manganite interfaces”, S. J. May, Telluride Workshop on Competing Interactions and Colossal Responses in Transition Metal Compounds, Telluride, CO, June 8-12, 2015.
15. “Fluorination of epitaxial oxides: Creating ferrite and nickelate oxyfluoride films” E. J. Moon, Y. J. Xie, D. J. Keavney, J. Goebel, E. D. Laird, C. Y. Li, and S. J. May. Nano, Polar, and Inorganic/Organic Materials: New Vistas in Photovoltaics Symposium, Philadelphia, PA, June 17, 2015.
- 16.\*“Control of magnetic oxide interfaces through engineering octahedral distortions” E. J. Moon. Joint MMM/Intermag conference, San Diego, CA, January 11-15, 2016.

**Number of Presentations:** 16.00

---

**Non Peer-Reviewed Conference Proceeding publications (other than abstracts):**

Received

Paper

**TOTAL:**

**Number of Non Peer-Reviewed Conference Proceeding publications (other than abstracts):**

---

**Peer-Reviewed Conference Proceeding publications (other than abstracts):**

Received

Paper

**TOTAL:**

**Number of Peer-Reviewed Conference Proceeding publications (other than abstracts):**

---

**(d) Manuscripts**

Received      Paper

- 04/10/2014 5.00 E. J. Moon,, S. J. May, P. V Balachandran, , B. J. Kirby,, D. J. Keavney,, R. J. Sichel-Tissot,, C. M. Schlepütz, , E. Karapetrova, , X. M. Cheng, , J. M. Rondinelli,. Effect of interfacial octahedral behavior in ultrathin manganite films,  
Nano Letters (01 2014)
- 04/10/2014 6.00 E. J. Moon, D. J. Keavney, S. J. May. Strain effects in narrow bandwidth manganites: The case of epitaxial Eu<sub>0.7</sub>Sr<sub>0.3</sub>MnO<sub>3</sub> thin films,  
PHYSICAL REVIEW Applied (03 2014)
- 04/27/2015 12.00 Qian He, R. Ishikawa, A.R. Lupini, L. Qiao, Eun Ju Moon, O. Ovchinnikov, Steven J. May , Michael D. Biegalski, AlbinaY. Borisevich. Towards 3D mapping of BO<sub>6</sub> octahedron rotations at perovskite heterointerfaces, unit cell by unit cell,  
Proceedings of the National Academy of Sciences (03 2015)
- 05/19/2015 13.00 Eun Ju Moon, Amber K. Choquette, Amanda Huon, Sam Z. Kulesa, Dmitri Barbash, Steven J. May. Comparison of topotactic fluorination methods for complex oxide films,  
APL Materials (02 2015)
- 08/15/2014 10.00 Eun Ju Moon, Robert Colby, Qiang Wang, Evguenia Karapetrova, Christian Schleputz, Michael Fitzsimmons, Steven May. Spatial control of functional properties via octahedral modulations in complex oxide superlattices,  
Nature Communications (submitted) (08 2014)
- 08/23/2013 1.00 Eun Ju Moon, David J. Keavney, Steven J. May. Strain-tailored magnetic phase transitions in epitaxial Eu<sub>0.7</sub>Sr<sub>0.3</sub>MnO<sub>3</sub> thin films,  
Appl. Phys. Lett. (submitted) (08 2013)
- 10/29/2013 2.00 Anand Bhattacharya, Steven May. Magnetic Oxide Heterostructures,  
Annual Review of Materials Research submitted (10 2013)
- 10/29/2013 3.00 Eun Ju Moon, Yujun Xie, Eric Laird, David Keavney, Christopher Li, Steven May. Fluorination of epitaxial oxides: Synthesis of perovskite oxyfluoride thin films,  
Journal of the American Chemical Society submitted (10 2013)
- TOTAL:**      **8**

**Number of Manuscripts:****Books**Received      Book**TOTAL:**Received      Book Chapter**TOTAL:****Patents Submitted****Patents Awarded****Awards**

The PI is the 2015 recipient of the Bradley Stoughton Award for Young Teachers. This is awarded by ASM International for outstanding teaching/mentoring in materials science and engineering to an individual under the age of 35.

**Graduate Students**

<u>NAME</u>	<u>PERCENT SUPPORTED</u>	Discipline
Alex Krick	0.02	
Hanqi Wu	0.04	
<b>FTE Equivalent:</b>	<b>0.06</b>	
<b>Total Number:</b>	<b>2</b>	

**Names of Post Doctorates**

<u>NAME</u>	<u>PERCENT SUPPORTED</u>
Eun Ju Moon	1.00
<b>FTE Equivalent:</b>	<b>1.00</b>
<b>Total Number:</b>	<b>1</b>

### **Names of Faculty Supported**

<u>NAME</u>	<u>PERCENT_SUPPORTED</u>	National Academy Member
Steven May	0.04	
<b>FTE Equivalent:</b>	<b>0.04</b>	
<b>Total Number:</b>	<b>1</b>	

### **Names of Under Graduate students supported**

<u>NAME</u>	<u>PERCENT_SUPPORTED</u>	Discipline
Yujun Xie	0.00	Materials Science and Engineering
Sam Kusela	0.00	Materials Science and Engineering
<b>FTE Equivalent:</b>	<b>0.00</b>	
<b>Total Number:</b>	<b>2</b>	

### **Student Metrics**

This section only applies to graduating undergraduates supported by this agreement in this reporting period

The number of undergraduates funded by this agreement who graduated during this period: ..... 1.00

The number of undergraduates funded by this agreement who graduated during this period with a degree in science, mathematics, engineering, or technology fields:..... 1.00

The number of undergraduates funded by your agreement who graduated during this period and will continue to pursue a graduate or Ph.D. degree in science, mathematics, engineering, or technology fields:..... 1.00

Number of graduating undergraduates who achieved a 3.5 GPA to 4.0 (4.0 max scale):..... 1.00

Number of graduating undergraduates funded by a DoD funded Center of Excellence grant for Education, Research and Engineering:..... 0.00

The number of undergraduates funded by your agreement who graduated during this period and intend to work for the Department of Defense ..... 0.00

The number of undergraduates funded by your agreement who graduated during this period and will receive scholarships or fellowships for further studies in science, mathematics, engineering or technology fields: ..... 0.00

### **Names of Personnel receiving masters degrees**

<u>NAME</u>
Yujun Xie
<b>Total Number:</b>

### **Names of personnel receiving PHDs**

NAME

**Total Number:**

### **Names of other research staff**

<u>NAME</u>	<u>PERCENT_SUPPORTED</u>
<b>FTE Equivalent:</b>	
<b>Total Number:</b>	

### **Sub Contractors (DD882)**

**Inventions (DD882)**

**Scientific Progress**

See Attachment

**Technology Transfer**

Symmetry mismatched heterostructures: New routes to bandwidth control in oxides  
Final Technical Report  
W911NF-12-1-0132  
PI: Steven May (Drexel University)

Period of Performance: 4/15/2012 – 4/14/2015

### Project Goals

This project aimed to discover novel physical phenomena in correlated  $ABO_3$  oxide heterostructures by using interfacial coupling to control the rotations and distortions of  $BO_6$  octahedra, the connectivity of which are directly coupled to electronic bandwidth. Related to this overall theme, there were three specific objectives identified in the proposal:

1. Demonstrate the direct role of a substrate's octahedral rotations on the electronic and magnetic properties of ultrathin films.
2. To stabilize superstructures of octahedral rotations that result in periodic bandwidth modulations. These spatial modulations of the octahedral rotations, and therefore electronic bandwidth, will be tuned by systematically adjusting the superlattice period, thereby providing a new means to spatially confine magnetic and electronic behavior.
3. To develop new experimental methods to depth-resolve octahedral rotations in oxide heterostructures.

### Scientific Accomplishments

#### **1. The effect of interfacial octahedral coupling in ultrathin manganite films**

The first object was to demonstrate the direct role of a substrate's octahedral rotations on the electronic and magnetic properties of correlated oxide films. To accomplish this objective, my group synthesized ultrathin films of  $La_{2/3}Sr_{1/3}MnO_3$  (LSMO) on  $(LaAlO_3)_{0.3}(Sr_2AlTaO_6)_{0.7}$  (LSAT) and  $NdGaO_3$  (NGO) substrates. These two substrates have approximately the same lattice parameter, ensuring that the films will be under equivalent strain states, but different crystal symmetries. In particular, LSAT lacks octahedral rotations while NGO exhibits the  $a\bar{a}c^+$  rotation pattern, as described by Glazer notation. In contrast, bulk LSMO exhibits the  $\bar{a}\bar{a}\bar{a}$  rotation pattern. We hypothesized that non-equilibrium symmetries can be induced in the LSMO via interfacial coupling with the substrate as shown in **Fig. 1(a)**, thereby providing a direct means to explore the role of the rotation pattern on electronic behavior.

Epitaxial LSMO films were grown on LSAT and NGO using ozone-assisted molecular beam epitaxy. A series of film growths targeting 5, 8, 11, 18, and 21 unit cells (uc) was carried out simultaneously on a LSAT, NGO (001), and NGO (110) substrates. The atomic fluxes were calibrated using Rutherford backscattering spectroscopy (RBS) and x-ray reflectivity (XRR). Following growth, XRR was also used to determine the film thicknesses. Additional structural information comes from synchrotron x-ray diffraction experiments carried out at Sector 33-BM at the Advanced Photon Source in collaboration with Jenia Karapetrova and Christian Schleputz. These results are presented in **Fig. 1(b)**, which shows data from the 11 uc films. The (002) diffraction peak appears at the same position for all films, verifying that they have the same nominal lattice parameters (ie. same strain state). In order to confirm that the films are all isocompositional, and thus changes in chemistry aren't dominating physical properties, x-ray absorption spectroscopy (XAS) measurements were performed at Sector 4-ID-C at the Advance Photon Source in collaboration with Dave Keavney. As shown in **Fig. 1(c)**, these results confirm that the nominal valence is the same in films of the same thickness.

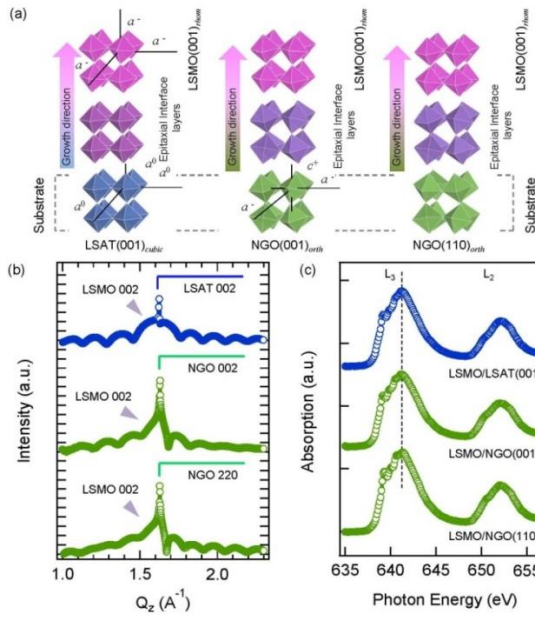


**Fig. 1.** Schematic of the LSMO/LSAT and LSMO/NGO heterostructures, highlighting the anticipated difference in  $\text{MnO}_6$  octahedral rotations (a). Synchrotron x-ray diffraction confirms that the films have the same lattice constants (b); x-ray absorption spectroscopy confirms that the films are in the same Mn valence state (c). These results serve as evidence that we have isolated octahedral coupling as the independent variable and that composition and strain are not driving the observed differences in physical properties.

The temperature-dependent resistivity of the films is shown in **Fig. 2(a)**. At 21 uc, the three LSMO films exhibit similar transport behavior independent of the substrate. This confirms that the physical properties of these films are dominated by strain and not interfacial structural coupling. This is consistent with a previous report of 55 uc LSMO films on LSAT and NGO [APL **95**, 112504 (2009)], which exhibited the same properties. As the thickness is reduced, the contribution from the interfacial region increases. At 11 uc and less, the low temperature resistivity varies by orders of magnitude with the LSMO/LSAT film always exhibiting the lowest resistivity. Additionally, the resistivity of manganites often exhibits a local maximum associated with the ferromagnetic transition ( $T_C$ ). These maxima are observed in the films. For instance at 11 uc,  $T_C \sim 300, 240$ , and  $170$  K for the LSMO/LSAT, LSMO/NGO (001), and LSMO/NGO (110), respectively, as determined from resistivity. The  $T_C$  can also be determined from magnetoresistance (MR) measurements, which were measured in a 7 T field. **Fig. 2(b)** shows the absolute value of the MR, defined as  $(R_{H=0} - R_{H=7T})/R_{H=0}$ . Similar to the resistivity, the  $T_C$  values for the 21 uc films are all similar but there is a wide range of  $T_C$  values for the 11 uc films.

To gain some insight into the length scale associate with the interfacial octahedral coupling, polarized neutron reflectometry (PNR) measurements were made on 18 uc films grown on each substrate. Reflectivity was measured to a high  $q$  value ( $0.2 \text{ \AA}^{-1}$ ), enabled by the high quality of the films, to increase depth resolution. The results and fits are shown in **Fig. 3(a-c)**. The obtained magnetic depth profile is given in **Fig. 3(d)**. The gray line shows the nuclear depth profile from the LSMO/LSAT film. The chemical interfacial width is  $\sim 10 \text{ \AA}$ . In contrast the magnetic width is much larger, with a reduced magnetization present in the first 4-5 uc ( $\sim 16\text{-}20 \text{ \AA}$ ) of the films. The width of this interfacial region is

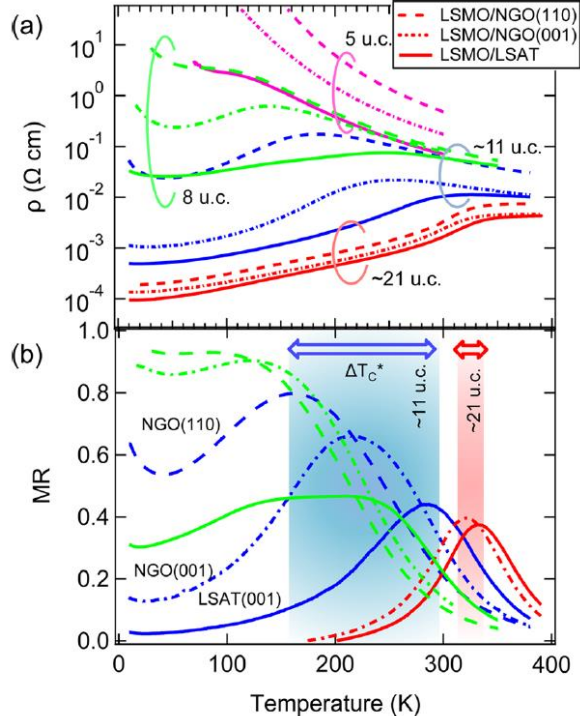


**Fig. 2.** Resistivity (a) and magnetoresistance (b) as a function of temperature for LSMO films of different thicknesses. While the 21 uc films on LSAT and NGO exhibit comparable properties, the thinner films exhibit systematic differences. Note that the films on LSAT have considerably lower resistivities and higher  $T_C^*$ , as determined from the temperature at which the MR is maximized.

approximately the same for all films; however, the LSMO/LSAT film has a larger magnetization than the films on NGO.

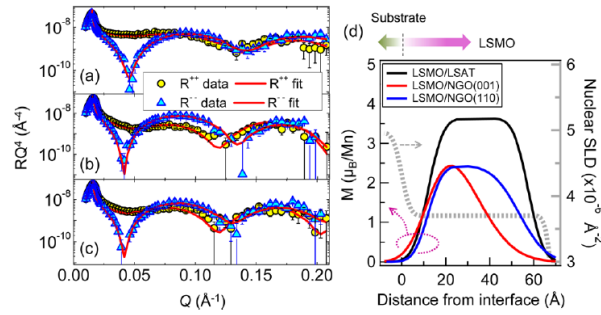


**Fig. 3.** Polarized neutron reflectometry results and fits from 18 uc LSMO films on LSAT (a), NGO (001) (b), and NGO (110) (c). The data was measured at 100 K in a 0.5 T field. The obtained magnetic depth profile across the film/substrate interface is shown in (d). The magnetic profile differs substantially from the nuclear profile indicating that changes in magnetization near the interface are not due to compositional changes. All the films exhibit a reduced magnetization in the ~4-5 uc nearest the interface. The film on LSAT exhibits the largest magnetization.

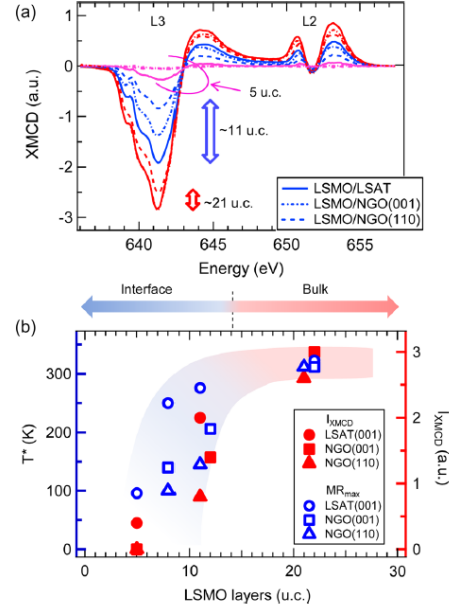


**Fig. 4.** Magnetic x-ray circular dichroism data from a series of 20, 11, and 5 uc thick LSMO films. In the 5 and 11 uc films, the LSAT has a substantially larger magnetic signal than the films on NGO.

The final characterization technique performed was magnetic x-ray circular dichroism (XMCD), in which the signal is proportional to the magnetization. This is necessary because conventional magnetometry measurements are unable to accurately measure the magnetization in the ultrathin LSMO films due to the reduced sample volume and a large signal from the NGO substrates. Furthermore, XMCD can probe element-specific magnetization. The XMCD measurements were also performed at Sector 4-ID-C at the Advanced Photon Source. Consistent with the resistivity and PNR results, the XMCD shows a systematically larger magnetization in the films on LSAT compared to NGO (**Fig. 4(a)**), which becomes especially apparent in the thinnest films. The experimental results are summarized in **Fig. 4(b)**, which shows the T<sub>c</sub> values obtained from MR and the XMCD intensities as a function of film thickness. A clear divergence is observed in the thinnest films between those grown on LSAT and those grown on NGO.

To further verify that the origin of this behavior is structural, first principles density functional theory calculations were performed by James Rondinelli's group. The DFT results show structural changes in the near-interfacial region of LSMO films on cubic and orthorhombic substrates are consistent with a suppression of octahedral at the junction with a cubic substrate. Corresponding calculations of the layer-resolved electronic structure reveals a reduced electronic bandwidth in the film on the orthorhombic substrate. These results are consistent with the hypothesis that the origin of the enhanced electronic/magnetic properties in LSMO/LSAT compared to LSMO/NGO is the reduced octahedral rotations in the near-interfacial region of the film. This work was published in *Nano Letters* and was chosen as a research highlight featured in the NIST Center for Neutron Scattering's 2014 annual report.

## 2. Bandwidth modulations in symmetry mismatched superlattices

Electronic and magnetic phenomenon in bandwidth modulated, isovalent superlattices was explored through the creation of multilayers in which the constituent materials have different octahedral rotations. The materials chosen for this study were  $(La_{0.7}Sr_{0.3}MnO_3)/(Eu_{0.7}Sr_{0.3}MnO_3)$  (LSMO)/(ESMO) superlattices. LSMO is a rhombohedral perovskite with the  $\bar{a}\bar{a}\bar{a}$  rotation pattern, while ESMO is a highly distorted orthorhombic perovskite with the  $\bar{a}\bar{a}\bar{c}^+$  rotation pattern. The first step in this project was optimizing the synthesis of ESMO, which had never been reported in epitaxial thin film form.

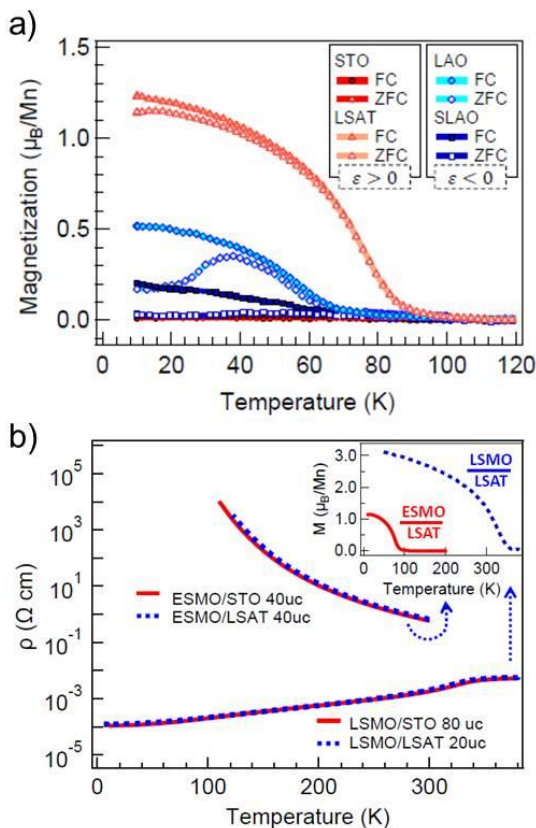


**Fig. 5.** The magnetic properties of ESMO films are highly sensitive to strain (a), while the electronic behavior is robustly insulating (b). This is in contrast to wide-bandwidth LSMO, which is metallic even under large epitaxial strains.

These superlattices are ideally suited for studying the effects of interfacial octahedral coupling at correlated interfaces because the Mn valence is uniform throughout the superlattice, thereby removing any effects from charge transfer that might complicate interpretation of the physical properties. In bulk, the  $MnO_6$  octahedral rotations lead to Mn-O-Mn bond angles ( $\theta$ ) of  $166.3^\circ$  and  $157^\circ$  in LSMO and ESMO, respectively, giving rise to larger electronic bandwidth in LSMO compared to ESMO. When epitaxially joined in superlattices, the atomic structure in the ESMO and LSMO layers will depend on the superlattice period ( $2n$ ) and the length scale for interfacial coupling of octahedral rotations ( $\zeta_0$ ). If the layer thickness is greater than  $\zeta_0$ , then the non-interfacial regions of LSMO and ESMO will exhibit differences in rotation angle due to their differences in bulk structure ( $\Delta\theta = \theta_{LSMO} - \theta_{ESMO}$ ). However, as the interfaces are brought closer together, making  $\zeta_0$  comparable to or greater than  $n$ , the structure of the layers will be increasingly dictated by the interfacial octahedral coupling, reducing the magnitude of  $\Delta\theta$ .

Optimal conditions for ESMO were identified using RBS to confirm cation composition, XRD to confirm crystalline quality and strain state, XAS to verify the Mn valence state, and XRR to quantify film thickness. We find that the magnetic properties of ESMO are highly strain dependent, shown in **Fig. 5(a)**. For instance, films on LSAT (0.6% tensile strain) are ferromagnetic with a  $T_C$  of  $\sim 80$  K, while films on  $SrTiO_3$  (1.5% tensile strain) are paramagnetic. In contrast to the magnetic behavior, we find that the electronic properties are not sensitive to strain, shown in **Fig. 5(b)**. Films with strain states ranging from -2.4 to 1.5 % all exhibit insulating behavior with little difference between the ferromagnetic film on LSAT, weakly ferromagnetic films on  $LaAlO_3$  and  $SrLaAlO_4$ , and paramagnetic film on  $SrTiO_3$ . Below  $\sim 120$  K, all films become too insulating for our measurement capabilities. The resistivity of ESMO follows simple Arrhenius behavior with an activation energy of 150 meV. This high magnetic sensitivity to strain and robust insulating behavior distinguishes narrow-bandwidth ESMO films from their wide-bandwidth LSMO counterparts, as in general the combination of ferromagnetism and insulating behavior is rare. The growth and characterization of ESMO films was published in *Physical Review Applied*.

Having established growth conditions for high quality ESMO, our work shifted to  $(LSMO)_n/(ESMO)_n$  superlattices grown on LSAT.

Thus, by tuning  $n$ , we can control the amplitude and period of octahedral modulations in the heterostructures. Octahedral modulations in the superlattices will produce modulations of electronic bandwidth, and functional properties dependent on bandwidth, such as magnetic exchange and electronic conduction. The design and control of octahedral modulations thus provides a unique opportunity to spatially confine functional behavior in perovskite oxides without relying on charge transfer.

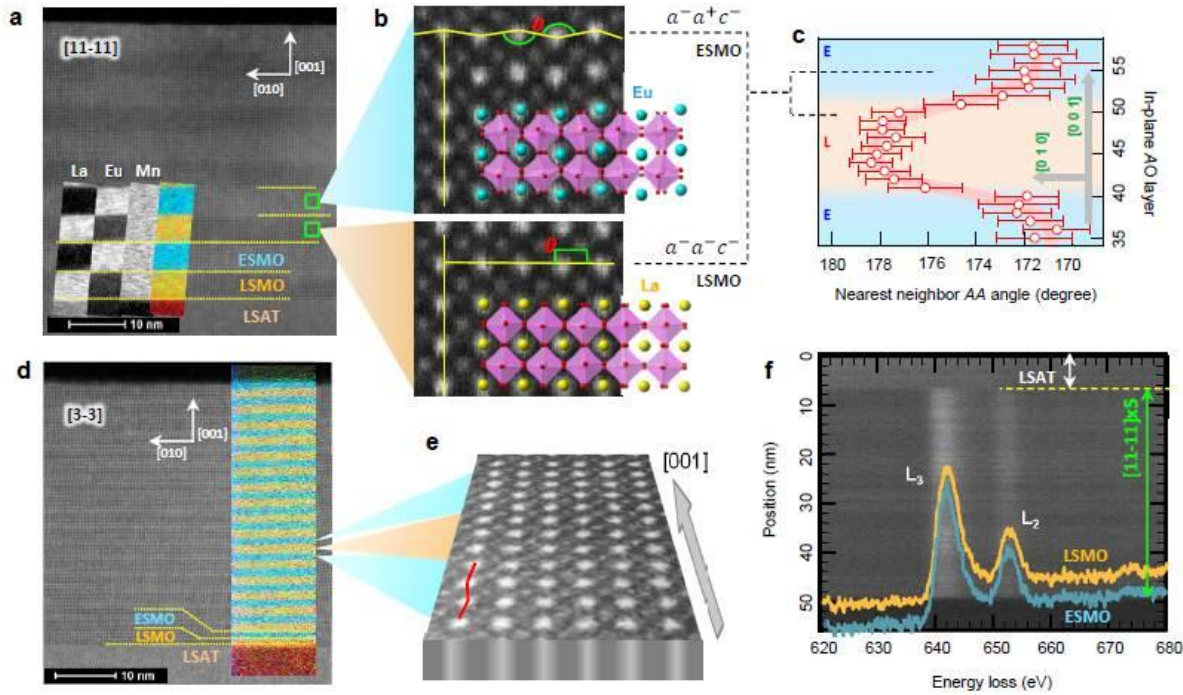


**Fig. 6.** (a) STEM image and EELS map of  $[n=11] \times 5$  superlattice grown on LSAT. (b) Enlarged images from typical LSMO (orange) and ESMO (blue) layers showing A-site displacements, highlighted with the yellow line. A schematic of the crystal structure is superimposed. (c) A-site displacement angles measured between three successive A-site columns along  $[010]$ . (d) STEM image and EELS map of the  $[n=3] \times 17$  superlattice. (e) Perspectively enlarged STEM image from three adjacent ESMO/LSMO layers showing A-site displacements across the SL interfaces. (f) EELS profile for the Mn L-edge from the  $n = 11$  sample with superimposed averaged Mn L-edge spectra for the non-interfacial regions of the ESMO and LSMO. The Mn  $L_{2,3}$  edge positions and shapes are consistent throughout SL film indicating a constant nominal Mn valence state across the LSMO/ESMO layers.

The structural quality of the superlattices has been confirmed with scanning transmission electron microscopy (STEM), performed by Bob Colby at Pacific Northwest National Laboratory, and synchrotron x-ray diffraction. The STEM measurements were carried out with electron energy loss spectroscopy (EELS) to provide local compositional information. **Figure 6** highlights the STEM-EELS results. The STEM-EELS confirms the superlattice structure with clear interfaces between the LSMO and ESMO layers, as shown in **Fig. 6(a)** for a  $n = 11$  sample and **Fig. 6(d)** for a  $n = 3$  sample. The A-site atoms are clearly resolvable; analysis of the A-site positions in the  $n = 11$  sample [**Fig. 6(b)**] reveals the presence of A-site displacements in the ESMO layers consistent with its bulk  $Pbnm$ -type orthorhombic structure. In contrast, A-site displacements are lacking in the LSMO layers. The A-A-A displacement angle was quantified, revealing that a region of  $\sim 4$  unit cells over which the structural coupling between ESMO and LSMO takes place [**Fig. 6(c)**]. The displacements also indicate that the ESMO layers have an  $a^-a^+c^-$  rotation pattern with the in-phase axis lying in-the-plane of the film. In contrast, the in-phase axis of the  $n = 3$  sample lies out-of-the-plane ( $a^-a^+$ ) [**Fig. 6(e)**]. The origin of this rotation-axis switch is currently unknown. Finally, EELS measurements of the Mn L-edge indicate a homogeneous Mn valence

throughout the superlattice [Fig. 6(f)], confirming that physical properties described below arise from structural modulations and not charge-based effects.

Synchrotron diffraction provides further evidence of the interfacial integrity of the superlattices and allows for measurement of the octahedral behavior within the samples. **Fig 7(a)** shows synchrotron diffraction measurements along the  $(0\ 0\ L)$  truncation rod of the  $n = 3, 6$ , and  $11$  superlattices. Satellite peaks are observed for all superlattices, confirming that the LSMO layers remain distinct from the ESMO layers. The measured data are in agreement with simulations (red solid lines), in which the superlattice is modeled as perfectly crystalline with atomically abrupt interfaces. In the simulation, the numbers of unit cells for both LSMO and ESMO were fixed to  $n = 3, 6$ , and  $11$ .

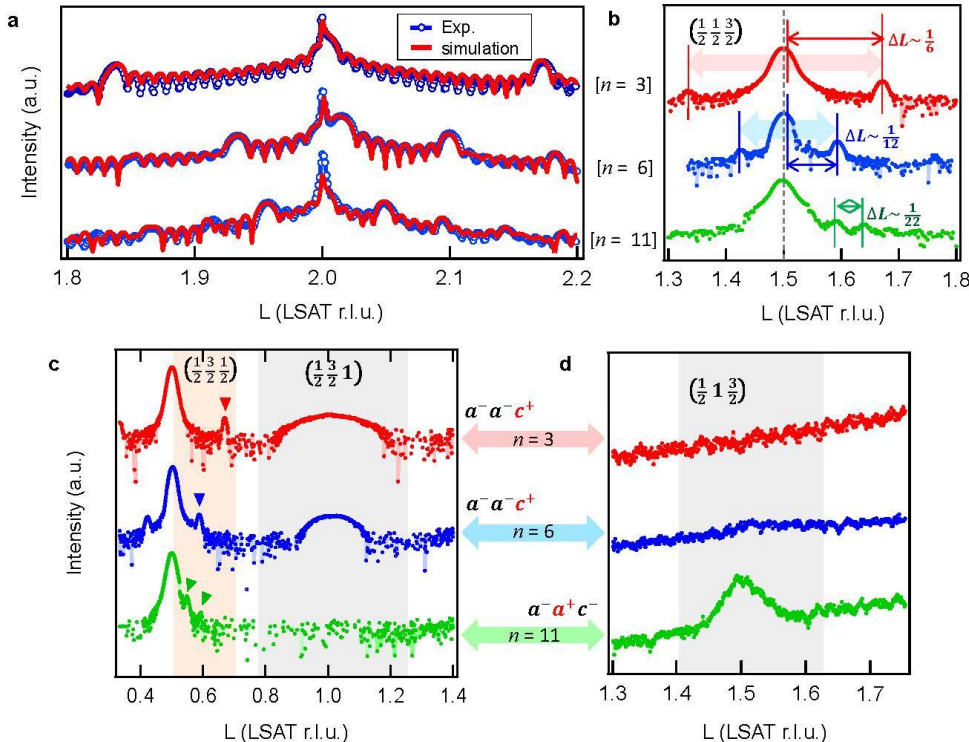


**Fig. 7.** (a) XRD data along the  $(00L)$  in the  $n = 3, 6$ , and  $11$  samples, exhibiting distinct satellite peaks due to the coherent SL structure. Red lines show the corresponding simulations. (b) Half-order satellite peaks near the  $(1/2\ 1/2\ 3/2)_{SL}$  reflection arising from modulations in the amplitude of the octahedral rotations along the growth direction. The distance between two satellite peaks ( $\Delta L$ ) confirms the period of the octahedral superstructure is the same as the chemical period of the superlattice. The LSAT substrate exhibits a broad, intense  $(1/2\ 1/2\ 3/2)$  peak, which obscures the principle  $(1/2\ 1/2\ 3/2)$  peak from the superlattice. (c) The  $(1/2\ 3/2\ 1)_{SL}$  reflection is observed in  $n = 3$  and  $n = 6$  samples, indicating the presence of an  $a^-a^-c^+$  rotation pattern. (d) The  $(1/2\ 1\ 3/2)_{SL}$  reflection is observed only in  $n = 11$  sample, indicating an  $a^-a^+c^-$  pattern.

In these samples, quantitative analysis of the half-order peak intensities is not possible due to the overlapping signal from the film and the intense peaks from the LSAT substrate. However, satellite peaks off of the  $(1/2\ 1/2\ 3/2)$  peaks along  $L$  were measured for the superlattices. These satellite peaks arise from modulations of the amplitude of the octahedral rotations along the growth direction. For instance, in **Fig. 7(b)**, a satellite peak is visible near  $L = 1.66$  for the  $n = 3$  SL. The distance between the  $(1/2\ 1/2\ 3/2)$  and the first satellite peak is  $\Delta L \sim 1/6, 1/12$ , and  $1/22$  for the  $n = 3, 6$ , and  $11$  samples. The presence of these satellite peaks at these positions in momentum space confirms that the period of the rotational superstructure is the same as the compositional period of the superlattices, consistent with the scenario presented in Fig. 5(a).

In addition to confirming the presence of rotational modulations, measurement of the half-order peaks were used to identify the dominant rotation pattern present in each superlattice. As shown in **Fig. 7(c)**, half-order (1/2 3/2 1) reflections were observed only in the  $n = 3$  and 6 samples. The presence of this peak indicates an  $a^-a^+c^+$  rotation, a result consistent with the A-site displacements observed in the STEM imaging. Additionally, the widths of these peaks along  $L$  yield correlation lengths that increase with increasing  $n$ .

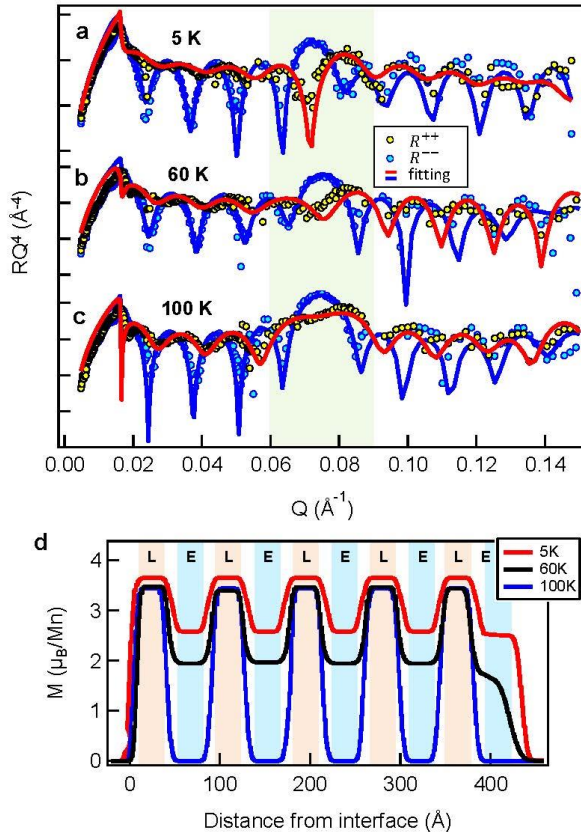


**Fig. 8.** Polarized neutron reflectivity multiplied by  $Q^4$  from the  $n = 11$  SL obtained at (a) 5 K, (b) 60 K, and (c) 100 K, measured with a 5000 Oe field in-the-plane of the films. Yellow and blue symbols (experimental data) indicate the reflectivity obtained with neutrons polarized parallel ( $R^{++}$ ) and antiparallel ( $R^{--}$ ) to the sample magnetization, respectively. (d) Obtained magnetic depth profiles of the sample corresponding to each temperature.

Vibrating sample magnetometry measurements were carried out on the  $n = 3$ , 6, and 11 superlattices. Although all three sample are similar in total thickness ( $\sim 100$  uc) and contained the same composition of LSMO and ESMO, the magnetization of the samples exhibit markedly different behavior, shown in **Fig. 9(a)**. The temperature-dependent magnetization of the  $n = 11$  sample exhibits a kink separating two regimes of magnetic behavior, a low temperature transition and a higher temperature transition. Similar behavior is found in the  $n = 6$  sample, but the inflection occurs at a higher temperature and the temperature of the second transition is reduced. Interestingly, a divided regime is not observed in the  $n = 3$  sample; instead, only a single transition is apparent.

However, the magnitude of the correlations lengths are slightly less than  $2n$ , indicating that in-phase rotations and A-site displacements that produce the (1/2 3/2 1) peak are not correlated through the superlattice but instead are only coherent within each ESMO layer. In contrast, the  $n = 11$  sample exhibits a (1/2 1 3/2) peak, as shown in **Fig. 7(d)**. This peak is indicative of an  $a^-a^+c^-$  rotation pattern, again consistent with the STEM imaging presented in Fig. 6(b).

Having established the presence of a periodic octahedral superstructure in the isovalent superlattices, the implications on the physical properties were investigated. We used polarized neutron reflectometry (PNR) to obtain a depth-resolved magnetic profile of the  $n = 11$  sample. These measurements were carried out at Lujan Neutron Scattering Center at Los Alamos in collaboration with Mike Fitzsimmons. The PNR data was collected in a saturating magnetic field at 5, 60, and 100 K. The data and best fits at each temperature are shown in **Fig. 8**. The reflectometry results confirm that the LSMO and ESMO layers are magnetically distinct in the  $n = 11$  sample, with the ESMO exhibiting a Curie temperature between 60 – 100 K, consistent with the  $T_C$  of ESMO films on LSAT. The thickness of the interfacial magnetic regions across the manganite heterojunctions is  $\sim 15$  Å, in good agreement with the thickness of the interfacial regions with varying A-site displacement angles obtained from STEM analysis [Fig. 6(c)].

To highlight the distinct transitions, the temperature derivative of the magnetization ( $dM/dT$ ) is shown in **Fig. 9(b)**. The  $dM/dT$  amplitude from the  $n = 11$  sample (in black) exhibits clear two minimum points at  $\sim 80$  and  $\sim 315$  K, consistent with the  $T_C$  of ESMO and LSMO films on LSAT, respectively. The presence of two transitions is also consistent with the PNR results. Similarly, the  $n = 6$  SL (in red) exhibits two minimum points at  $\sim 105$  and  $\sim 240$  K, indicating the transition temperatures of the ESMO and LSMO are shifted toward one another as the difference in octahedral rotations in the two constituent materials is reduced. In contrast to these, for the  $n = 3$  superlattice (in blue), the  $dM/dT$  reveals a single minimum point at  $\sim 190$  K, indicating one  $T_C$ . These results demonstrate that the magnetization of the individual layers can be tuned by controlling the magnitude of the rotational modulations throughout the superlattices even while the composition of the layers remains unchanged. In the  $n = 3$  superlattice, where the distance between interfaces is brought below the interfacial octahedral coupling length, a single  $T_C$  is observed consistent with a uniform octahedral structure despite the presence of the compositional superlattice. Importantly, a uniform alloy film of  $\text{La}_{0.35}\text{Eu}_{0.35}\text{Sr}_{0.3}\text{MnO}_3$  (in green) with the same composition as the superlattices exhibits significantly reduced  $T_C$  and magnetization compared to the  $n = 3$  sample (inset). This indicates that the magnetic behavior in the  $n = 3$  superlattice is not the same as a simple average of LSMO and ESMO, as exhibited in a random alloy film. We attributed the enhanced  $T_C$  in the superlattice to the suppression of cation site disorder, as variance in cation size is known to suppress  $T_C$  in bulk manganites. Additionally, the resistivity of the  $n = 3$  superlattice and random alloy are very different, with the superlattice exhibit orders of magnitude lower resistivity.

The transition from a modulated magnetic structure, confirmed by PNR, to a uniform magnetic structure, as indicated by the single transition temperature, is consistent with the structural modulations revealed by STEM and XRD. The STEM imaging reveals a structural coupling length of  $\zeta_0 \sim 4$  unit cells, a result consistent with the interfacial magnetic width obtained from PNR. As hypothesized, superlattices with  $n > \zeta_0$ , behave as the sum of the two constituent materials, while the  $n = 3$  superlattice behaves as a material with uniform magnetization. The observation that the  $T_C$  of the  $n = 3$  sample is between that of bulk LSMO and ESMO is in line with the expectation that the magnitude of the octahedral rotations are approximately the average of those found in LSMO and ESMO. While the  $T_C$  of the LSMO layers is reduced with decreasing  $n$ , the  $T_C$  of the ESMO layers is increased as the layer thickness is reduced: a result opposite to that expected from simple finite thickness effects. However, the increased  $T_C$  of the ESMO layers is fully consistent with an increase in  $\theta$  as  $n$  is reduced. These results directly demonstrate how engineering the local atomic structure of perovskites via the rational design of octahedral superstructures can be used to spatially tailor magnetization. This effect is analogous to delta doping strategies that have been pursued in oxide heterostructures; ***however, unlike charge-based doping, this structural “doping” approach has no analogue in conventional semiconductor heterostructures, and therefore represents a new paradigm for controlling physical behavior in complex oxide heterostructures.*** The implications of this work extend well beyond manganite superlattices, as the

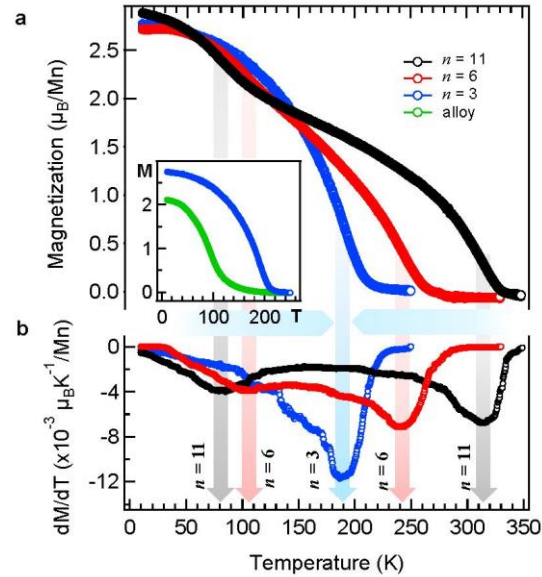


**Fig. 9.** Magnetization measurements of three superlattices. (a) M-T under a 500 Oe field applied in the plane of the  $n = 11$  (black), 6 (red), and 3 (blue) superlattices. (b) Corresponding derivative of the magnetization with respect to temperature obtained from (a). The downward arrows indicate the approximate transition temperatures. Inset shows an alloy film of  $\text{La}_{0.35}\text{Eu}_{0.35}\text{Sr}_{0.3}\text{MnO}_3$  (also 100 unit cells) in green to compare with the  $n = 3$  sample.

observed design strategy can be broadly applied to spatially confine and segregate electronic and ferroic properties in perovskite superlattices. This work was published in *Nature Communications*.

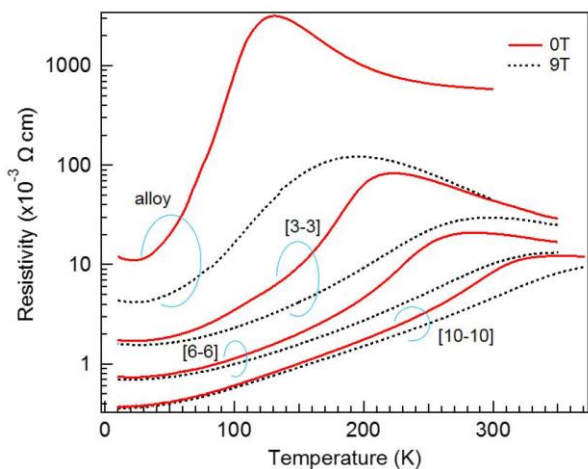


**Fig. 10.** Temperature dependent resistivity, with and without an magnetic field applied in-plane, measured in the  $n = 3, 6$ , and  $10$  superlattices and random alloy LSMO film on LSAT substrates.

magnetoresistance measurements.

In addition to the magnetic measurements, we have also performed electronic characterization of the superlattices. **Fig. 10** shows the temperature-dependent resistivity with and without a magnetic field from the samples. The random alloy is significantly more insulating than the superlattices. In the superlattices, as more adjacent LSMO layers are added, the resistivity is decreased and the temperature of the local resistivity maxima is increased. On this grant, we also carried out some preliminary anomalous Hall effect measurements that show an enhancement of the anomalous Hall effect in the superlattices. We hypothesize that the modulations of rotations lead to a modulated spin canting due to the Dzyaloshinskii-Moriya interactions that arises from octahedral rotations in perovskites. Future work is focused on patterning the samples into Hall bar geometries for more precise Hall effect and anisotropic

### 3. New experimental methods for probing octahedral rotations

This project has led to two significant contributions to the depth-dependent characterization of octahedral rotations in oxide heterostructures. The first is the first reported measurement of satellite peaks off of half-order diffraction peaks. These satellite peaks, shown in Fig. 7(b,c), arise from modulations of the magnitude of octahedral rotations. As the half-order diffraction peaks are due to the rotations, any periodic spatial variation of the rotations leads to these superstructure peaks. These peaks are analogous to superlattice peaks observed in  $(00L)$  diffraction that arise from chemical/structural modulations; here, the origin of the modulations is spatially varying changes in the oxygen positions.

The second contribution came in collaboration with Qian He and Albina Borisevich at Oak Ridge National Laboratory. They developed a technique in which column shape analysis of annular bright field (ABF) scanning transmission electron microscopy (STEM) images taken along specific crystallographic orientations enable the determination of the three-dimensional rotation pattern at the unit cell level. As a test case, they applied this technique to the  $(\text{LSMO})_6/(\text{ESMO})_6$  superlattice grown on  $\text{SrTiO}_3$ .

Representative STEM high angle annular dark field (HAADF) and ABF images of the LSMO/ESMO interfaces are shown in **Fig. 11(a)**. The oxygen columns in both LSMO and ESMO regions all appear to be elliptical in shape, consistent with simulations of materials with octahedral rotations. A change in  $\gamma$  rotation phase can be visually detected as a mirror plane (shown as a yellow dashed line) that arises between adjacent oxygen columns along the out-of-plane direction. **Fig. 11(b)** shows the plane averaged inclination angle  $\theta$  (note, this  $\theta$  is not the same as the  $B$ - $O$ - $B$  rotation angle) of the major axes of the oxygen column ellipses as a function of coordinate along the out-of-plane direction. The emergence of “+”  $\gamma$  rotation in the ESMO layer is indicated by the  $\theta$  angle alternating signs. The magnitude of  $\theta$  appears constant within both LSMO and ESMO layers, with no interfacial effects, indicating that the  $\gamma$  rotation phase changes abruptly. This is possible as the phase of the  $\gamma$  rotation does not alter the position of the apical oxygen atom that bridges the two materials. The advantage of this method is its applicability to locally probe regions containing domains and defects, and that no material-specific simulation is required to obtain qualitative information on the tilt pattern. This work was published in *ACS Nano*.

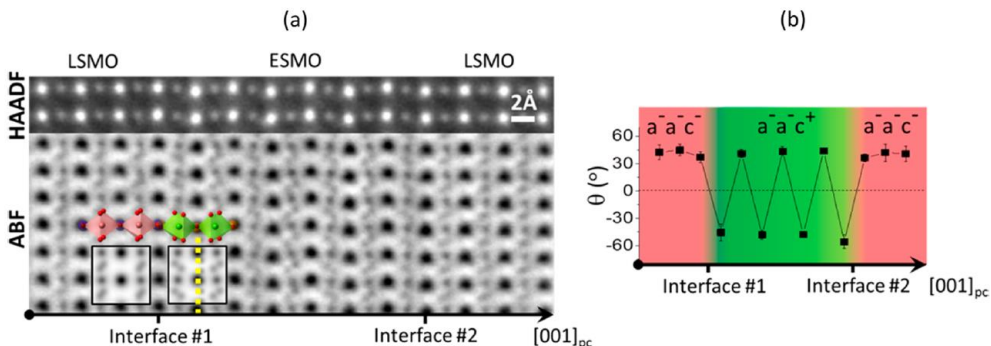


**Fig. 11.** The interface in the  $(\text{LSMO})_6/(\text{ESMO})_6$  superlattice. (a) Experimental STEM HAADF and ABF images of the LSMO/ESMO interfaces along one  $[110]_{pc}$  axis, with overlapped polyhedral model and the simulated ABF images (insets). (b) The plane averaged profile of  $\theta$ , the ellipsoid inclination angle, measured from the image in (a) with respect to the direction defined by adjacent  $B$  sites.

#### 4. Anionic substitution in epitaxial perovskite films

The final accomplishment of the project was developing a synthetic route to realizing oxyfluoride perovskite thin films. This work has the potential to open up an entirely new class of materials – mixed anion epitaxial perovskites – for study. The substitution of F for O on the anion site may provide an appealing alternative to oxygen vacancies as a means to electron dope perovskites. This work has been published in the *Journal of the American Chemical Society* and *APL Materials*.

The fluorination process was carried out on as-grown oxygen deficient films using two different approaches. In the first approach, the film is spin-coated (SC) with a solution of poly(vinylidene fluoride) (PVDF) (10 wt% in dimethylformamide (DMF)), which is followed by a heat treatment in a quartz tube under a slow  $\text{O}_2$  flow at  $600^\circ\text{C}$  for 2 hours (h) [Figure 12(a)]. The presence of  $\text{O}_2$  during the annealing step of the SC process facilitates the removal of the by-products produced during thermal decomposition of the PVDF. In contrast, when the SC process was performed under a  $\text{N}_2$  gas flow, a black residue remained on the film following the anneal and no film peaks were present in x-ray diffraction. Figure 12(b) illustrates the second approach, a vapor transport (VT) process. In this approach, fluorination is carried out by heating a perovskite film and PVDF pellets in a quartz tube for 24 h under a flowing carrier gas; here we use  $\text{N}_2$  and Ar. The film is placed in the quartz tube downstream from the PVDF pellets.

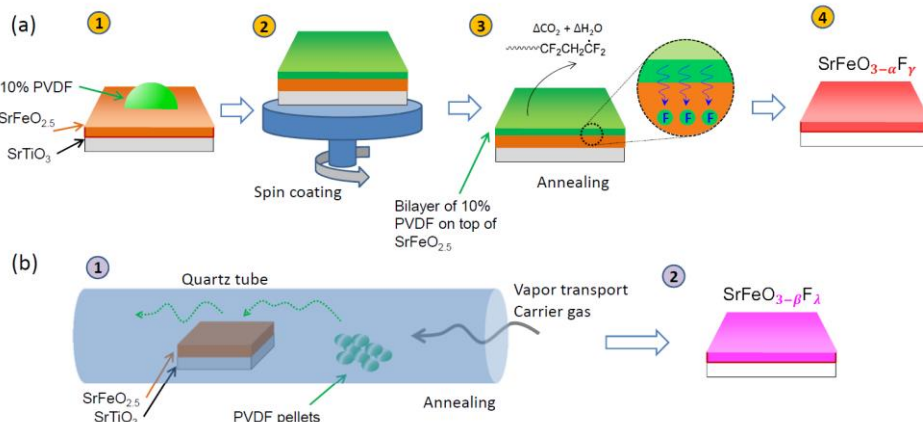


**Fig. 12.** Schematics of the fluorination processes. (a) Spin-coating process carried out on a bilayer consisting of PVDF and an oxygen-deficient  $\text{SrFeO}_{3-\delta}$  film. A PVDF solution is first spin-coated onto an oxygen-deficient  $\text{SrFeO}_{3-\delta}$  film grown on STO (1). After the heat treatment of fluorination process (2),  $\text{SrFeO}_{3-\alpha}\text{F}_\gamma$  is obtained (3). (b) Vapor transport process carried out on an as-grown  $\text{SrFeO}_{3-\delta}$  placed downstream from PVDF pellets in a heating quartz tube in the presence of a flowing carrier gas, resulting in  $\text{SrFeO}_{3-\beta}\text{F}_\lambda$ .

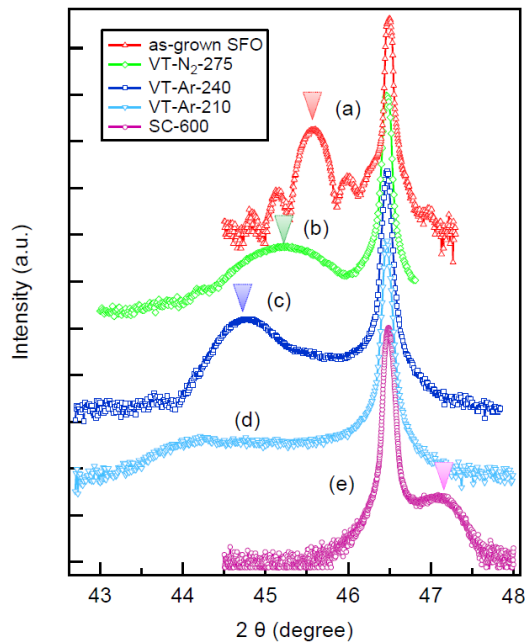


**Fig. 13.** X-ray diffraction from  $\text{SrFeO}_{2.5}$ ,  $\text{SrFeO}_3$ , and two  $\text{SrFeO}_{3-\delta}\text{F}_\gamma$  films measured about the (002) peak.

temperature range for the VT process. In contrast to the VT fluorination process, the film (0 0 2) peak from SFO-F film synthesized by the SC process (SC-600) appears at a higher angle than that of the STO substrate and its *c*-axis parameters is  $\sim 3.855 \text{ \AA}$  [Fig. 13(d)]. Films processed with the SC method at  $400^\circ\text{C}$  and  $800^\circ\text{C}$  did not exhibit diffraction peaks. The crystalline coherent length ( $\xi$ ) along the out-of-plane direction, obtained from XRD, for the fluorinated films is equal to 12, 18, and 10 nm for the VT-N<sub>2</sub>-275, VT-Ar-240, and SC-600 films, respectively, indicating that the crystalline quality of the VT synthesized films is better than that of the SC synthesized films.

The relative fluorine concentration as a function of distance from the surface was measured by x-ray photoemission depth profile analysis, performed with Ar+ sputtering of the film. These results reveal that the SC process leads to a more uniform F incorporation within the film. **Figure 14** shows the depth profiles of the O 1s, F 1s, Fe 2p, and Ti 2p normalized peak intensities. The depth at which the Fe 2p is suppressed and the Ti 2p peak appears indicates the relative location of the film/substrate interface. **Fig. 14(a)** shows the normalized concentration depth profile for the VT-Ar-210 film, revealing a near-surface region with a gradually decreasing F concentration, followed by a region of constant F concentration. Assuming the sputter rate is constant as a function of depth within the film, each of these two regions are  $\sim 12 \text{ nm}$ . When the VT processing temperature is raised to  $240^\circ\text{C}$  in Ar, the constant F concentration region is increased to  $\sim 17 \text{ nm}$ , while the near-surface of varying F content becomes less wide ( $\sim 5 \text{ nm}$ ), as shown in **Fig. 14(b)**. The depth profile from the VT-N<sub>2</sub>-275 sample is shown in **Fig. 14(c)**. This film also exhibits two layers of differing F concentration. The layer with constant F concentration is approximately the same width as that of VT-Ar-240 but with a seemingly lower F concentration. The depth profile of the SC-600 film [**Fig. 14(d)**] reveals a more uniform F concentration throughout the film, extending from the surface to a depth of  $\sim 15 \text{ nm}$ . The carbon 1s peak was also measured after each sputtering cycle to monitor carbon contamination. While the as-fluorinated VT and SC films have a C 1s peak at the surface, the peak is absent after 1 minute of sputtering.

**Figure 13** shows XRD measurements taken around the pseudocubic (0 0 2) truncation rod of strontium ferrite (SFO) films before and after the two different fluorination processes. The *c*-axis parameter of the as-grown oxygen deficient SFO thin film is  $\sim 3.979 \text{ \AA}$ , as shown in **Fig. 13(a)**, which is comparable to previous reports of brownmillerite  $\text{SrFeO}_{2.5}$  films on  $\text{SrTiO}_3$ . The XRD data of the film fluorinated with the VT method at  $275^\circ\text{C}$  in N<sub>2</sub> (hereafter, VT-N<sub>2</sub>-275) shows a Bragg peak corresponding to a *c*-axis parameter of  $\sim 4.004 \text{ \AA}$  [Fig. 13(b)]. The fluorinated film by VT in Ar gas at  $240^\circ\text{C}$  (VT-Ar-240) exhibits a diffraction peak of a *c*-axis parameter  $\sim 4.044 \text{ \AA}$  [Fig. 13(c)]. In the film fluorinated at the lower temperature of  $210^\circ\text{C}$  in Ar gas (VT-Ar-210), the Bragg peak is shifted further to a lower angle than the VT-Ar-240 film, but with much weaker intensity and significant peak broadening [Fig. 13(d)]. The VT process is very sensitive to the processing temperature. Films fluorinated in flowing N<sub>2</sub> did not exhibit a Bragg peak when the process was carried out below  $240^\circ\text{C}$  or above  $300^\circ\text{C}$ . Similarly, Bragg peaks were not observed for VT-processed films in flowing Ar for annealing temperatures above  $275^\circ\text{C}$ . Therefore, we find that the choice of carrier gas alters the optimal

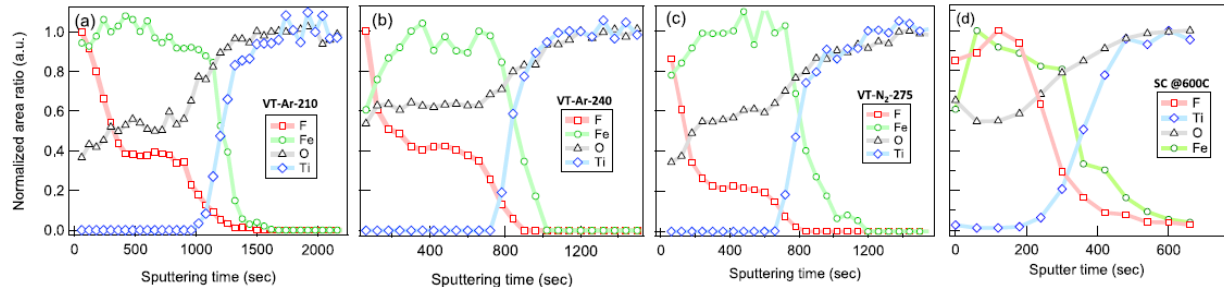


**Fig. 14.** Normalized concentration depth profiles obtained from XPS for four different SFO-F /STO films (a) VT-Ar-210 for 24 h, (b) VT-Ar-240 for 24 h, (c) VT-N<sub>2</sub>-275 for 24 h, and (d) SC-600 for 2 h.

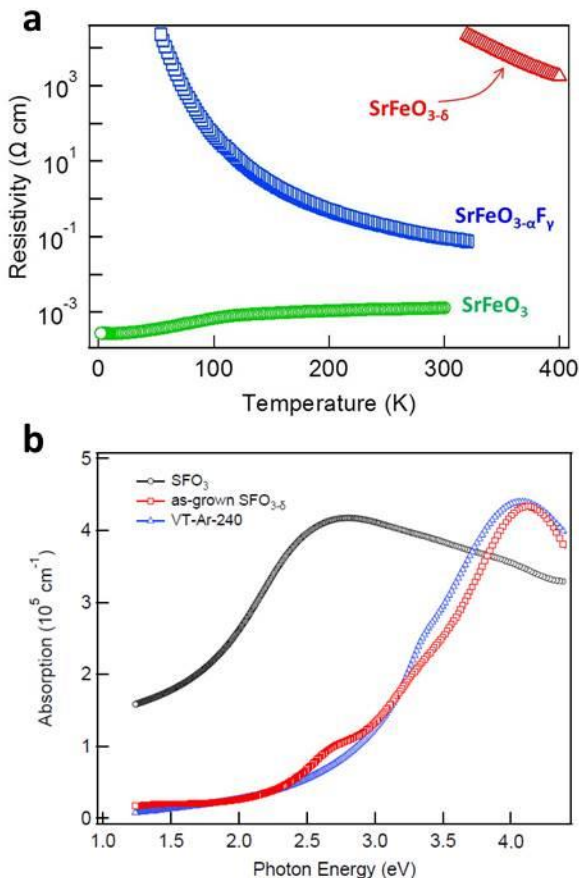


**Fig. 15.** (a) Resistivity of SrFeO<sub>2.5</sub> (red), SC-processed SrFeO<sub>3- $\delta$</sub> F $_{\gamma}$  (blue), and SrFeO<sub>3</sub> (green). (b) Optical absorption of SrFeO<sub>2.5</sub> (red), VT-processed SrFeO<sub>3- $\delta$</sub> F $_{\gamma}$  (blue), and SrFeO<sub>3</sub> (black).

The incorporation of F into the SFO leads to changes in the physical properties consistent with the presence of F<sup>-</sup> on the anion site. Temperature dependent resistivity of the SC processed film, in which F is believed to occupy ~1/6 of the anion sites leading to a nominal Fe valence near 3.5+, reveal conductivity behavior between that of SrFeO<sub>2.5</sub> (highly insulating) and SrFeO<sub>3</sub> (metallic) [Fig. 15(a)]. Optical absorption spectra of the VT process films, in which F is believed to occupy 1/3 of the anion sites leading to a nominal Fe valence of 3+, are very similar to SrFeO<sub>2.5</sub> films in which the Fe exhibits the same valence state [Fig. 15(b)].

The simplicity of the fluorination processes, and the fact that they can be performed on films deposited with any growth technique, makes these reactions readily adoptable by the oxide film community. It is anticipated that these results will open up an entirely new class of materials - mixed anion epitaxial perovskites - for study, and catalyze substantial efforts within the oxide films community to explore topotactic reactions as a means to expand the anionic chemistries accessible in perovskite heterostructures.

### Summary of Accomplishments

- Provided strong evidence that interfacial octahedral coupling is critical in controlling properties in ultrathin perovskite oxide films and heterostructures. This was accomplished by a systematic study of electronic and magnetic properties in  $\text{La}_{2/3}\text{Sr}_{1/3}\text{MnO}_3$  films grown on LSAT and  $\text{NdGaO}_3$ .
- Provided the first direct experimental demonstration of how octahedral behavior in oxide superlattices can be used to engineer spatially confined or uniform macroscopic properties by varying the superlattice period with respect to the length scale of interfacial structural coupling.
- Demonstrated that interfacial structural coupling can be used to tailor Curie temperatures in the individual ESMO and LSMO layers of  $\text{Eu}_{0.7}\text{Sr}_{0.3}\text{MnO}_3/\text{La}_{0.7}\text{Sr}_{0.3}\text{MnO}_3$  superlattices. Showed that the magnetic and electronic behavior of the superlattices differs substantially from an isocompositional random alloy film.
- Developed, directly or through collaborations, new experimental approaches for probing depth dependent octahedral rotations via measurement of half-order satellite diffraction peaks or bright field STEM imaging.
- Developed synthesis processes to realize oxyfluoride thin films, which we have been used to make  $\text{SrFeO}_{3-\delta}\text{F}_\gamma$  and  $\text{LaNiO}_{3-\delta}\text{F}_\gamma$ .
- Published 7 papers, 5 of which are in journals with impact factors greater than 10. Gave numerous invited talks, including at the APS March meeting, based on results from this project.

### Project-Funded Publications

1. “Magnetic oxide heterostructures”, A. Bhattacharya and S. J. May. *Annual Review of Materials Research* **44**, 65 (2014).
2. “Strain effects in narrow bandwidth manganites: The case of epitaxial  $\text{Eu}_{0.7}\text{Sr}_{0.3}\text{MnO}_3$  thin films”, E. J. Moon, D. J. Keavney, and S. J. May. *Physical Review Applied* **1**, 054006 (2014).
3. “Effect of interfacial octahedral behavior in ultrathin manganite films”, E. J. Moon, P. V. Balachandran, B. J. Kirby, D. J. Keavney, R. J. Sichel-Tissot, C. M. Schleputz, E. Karapetrova, X. M. Cheng, J. M. Rondinelli, and S. J. May. *Nano Letters* **14**, 2509 (2014).
4. “Fluorination of epitaxial oxides: Synthesis of perovskite oxyfluoride thin films”, E. J. Moon, Y. J. Xie, E. D. Laird, D. J. Keavney, C. Y. Li, and S. J. May. *Journal of the American Chemical Society* **136**, 2224 (2014).
5. “Spatial control of functional properties via octahedral modulations in complex oxide superlattices”, E. J. Moon, R. Colby, Q. Wang, E. Karapetrova, C. M. Schlepütz, M. R. Fitzsimmons, and S. J. May. *Nature Communications* **5**, 5710 (2014).
6. “Comparison of topotactic fluorination methods for complex oxide films”, E. J. Moon, A. K. Choquette, A. Huon, S. Z. Kusela, D. Barbash, and S. J. May. *APL Materials* **3**, 062511 (2015).
7. “Towards 3D mapping of  $\text{BO}_6$  octahedron rotations at perovskite heterointerfaces, unit cell by unit cell”, Q. He, R. Ishikawa, A. R. Lupini, L. Qiao, E. J. Moon, O. Ovchinnikov, S. J. May, M. D. Biegalski, and A. Y. Borisevich. *ACS Nano*, in press (2015). DOI: 10.1021/acsnano.5b03232

### Project-Funded Conference Presentations

\* denotes invited talk

The results from this project were presented at numerous invited departmental seminars given by the PI over the course of this reporting period. The ARO funding was acknowledged in all presentations.

- 1.\* "Measuring octahedral behavior in complex oxide heterostructures." S. J. May, workshop on Future Directions for Emergent Discoveries at Oxide Interfaces by Design, Newport, RI, July 9-10, 2012.
- 2.\* "Measuring and controlling octahedral behavior in oxide heterostructures." S. J. May, Complex Oxide Heterostructure Workshop at Harvard University, Cambridge, MA, August 8-9, 2012.
- 3.\* "Control of octahedral connectivity in oxide heterostructures" S. J. May, Materials Research Society fall meeting, Boston, MA, November 26 – 30, 2012.
4. "The effect of interfacial octahedral behavior on magnetic properties in ultrathin manganite films" E. J. Moon, X. Cheng, D. J. Keavney, and S. J. May. American Physical Society March meeting, Baltimore, MD, March 18 – 22, 2013.
5. "Fluorination of epitaxial oxides: Creating ferrite and nickelate oxyfluoride films" E. J. Moon, Y. J. Xie, D. J. Keavney, J. Goebel, E. D. Laird, C. Y. Li, and S. J. May. American Physical Society March meeting, Baltimore, MD, March 18 – 22, 2013.
- 6.\* "Anion-based approaches to tunable functionality in oxide heterostructures" S. J. May, Telluride Workshop on Competing Interactions and Colossal Responses in Transition Metal Compounds, Telluride, CO, July 15-19, 2013.
7. "Magnetic effect of interfacial octahedral behavior in ultrathin manganite films" E. J. Moon, B. J. Kirby, D. J. Keavney, P. V Balachandran, R. J. Sichel-Tissot, C. M. Schlepütz, E. Karapetrova, X. M. Cheng, J. M. Rondinelli, and S. J. May. Magnetism and Magnetic Materials conference, Denver, CO. November 4-8, 2013.
8. "Strain-tailored magnetic properties of epitaxially grown ultrathin  $\text{Eu}_{0.7}\text{Sr}_{0.3}\text{MnO}_3$  films" E. Moon, D. Keavney and S. May. Magnetism and Magnetic Materials conference, Denver, CO. November 4-8, 2013.
- 9.\* "The effect of interfacial octahedral behavior in ferromagnetic manganite heterostructures" E. J. Moon and S. J. May, American Ceramic Society Electronic Materials and Applications, Orlando, FL, January 22-24, 2014.
- 10.\* "Anion-based approaches to tunable functionality in oxide heterostructures" S. J. May, American Physical Society March meeting, Denver, CO, March 3-7, 2014.
- 11.\* "Anion-based approaches to tunable functionality in perovskite films and superlattices" S. J. May, 21<sup>st</sup> International Workshop on Oxide Electronics, Bolton Landing, NY, September 28–October 1, 2014.
12. "Spatial control of functional properties via octahedral modulations in complex oxide superlattices" E. J. Moon, R. Colby, Q. Wang, E. Karapetrova, C. M. Schleputz, M. R. Fitzsimmons, S. J. May. MRS Fall Meeting, Boston, MA, Dec. 1 – 4, 2014.
- 13.\* "Engineering anion positions and compositions in perovskite oxide heterostructures" S. J. May, International Conference on Electroceramics, State College, PA, May 13 – 16, 2015.
- 14.\* "Structural approaches for altering electronic and magnetic properties at manganite interfaces", S. J. May, Telluride Workshop on Competing Interactions and Colossal Responses in Transition Metal Compounds, Telluride, CO, June 8-12, 2015.
15. "Fluorination of epitaxial oxides: Creating ferrite and nickelate oxyfluoride films" E. J. Moon, Y. J. Xie, D. J. Keavney, J. Goebel, E. D. Laird, C. Y. Li, and S. J. May. Nano, Polar, and Inorganic/Organic Materials: New Vistas in Photovoltaics Symposium, Philadelphia, PA, June 17, 2015.
- 16.\* "Control of magnetic oxide interfaces through engineering octahedral distortions" E. J. Moon. Joint MMM/Intermag conference, San Diego, CA, January 11-15, 2016.